Wind and Structures, *Vol. 18, No. 5 (2014) 567-598*
DOI: http://dx.doi.org/10.12989/was.2014.18.5.567

Computational evaluation of wind loads on a standard tall building using LES

Ageneh K. Dagnew[1a] and Girma T. Bitsuamlak[*2]

[1]Research and Modeling, AIR Worldwide, 131 Dartmouth Street, Boston, MA, USA
[2]WindEEE Research Institute/Department of Civil and Environmental Engineering, University of Western Ontario in London, ON, Canada

(Received July 2, 2013, Revised December 20, 2013, Accepted February 18, 2014)

Abstract. In this paper, wind induced aerodynamic loads on a standard tall building have been evaluated through large-eddy simulation (LES) technique. The flow parameters of an open terrain were recorded from the downstream of an empty boundary layer wind tunnel (BLWT) and used to prescribe the transient inlet boundary of the LES simulations. Three different numerically generated inflow boundary conditions have been investigated to assess their suitability for LES. A high frequency pressure integration (HFPI) approach has been employed to obtain the wind load. A total of 280 pressure monitoring points have been systematically distributed on the surfaces of the LES model building. Similar BLWT experiments were also done to validate the numerical results. In addition, the effects of adjacent buildings were studied. Among the three wind field generation methods (synthetic, Simirnov's, and Lund's recycling method), LES with perturbation from the synthetic random flow approach showed better agreement with the BLWT data. In general, LES predicted peak wind loads comparable with the BLWT data, with a maximum difference of 15% and an average difference of 5%, for an isolated building case and however higher estimation errors were observed for cases where adjacent buildings were placed in the vicinity of the study building.

Keywords: LES; BLWT; inflow turbulence; wind force coefficients; power spectrum; tall building

1. Introduction

Several wind load evaluation studies for buildings in boundary layer wind tunnels have been reported by various researchers, and more recently through a numerical approach. Recent advances in hardware and software technology coupled with the development of reliable sub-grid turbulence models and numerical generation of inflow turbulence, which replicates upstream conditions, is making a computational wind load evaluation an attractive proposition (Tamura *et al.* 2008, Tominaga *et al.* 2008, Huang and Li 2010, Dagnew and Bitsuamlak 2013). Previous numerical studies have focused on both short and tall buildings. Some of the numerically studied full-scale, low-rise buildings included the Silsoe Cube (Wright and Easom 2003), Texas Tech Building (Senthooran *et al.* 2004) and the Wall of Wind Test Building (Bitsuamlak *et al.* 2010). Studies on high-rise buildings include the research by Nozawa and Tamura (2003), who predicted the

---

[*] Corresponding author, Associate Professor, E-mail: gbitsuam@uwo.ca
[a] Research Engineer

http://www.techno-press.org/?journal=was&subpage=8 ISSN: 1226-6116 (Print), 1598-6225 (Online)

time-averaged pressure coefficients on a high-rise building (1:1:4) using LES, and the work of Tamura *et al.* (2008), which highlighted the guidelines of the Architectural Institute of Japan (AIJ) for the numerical prediction of wind loads. Huang *et al.* (2007) and Braun and Awruch (2009) studied the external aerodynamics of a standard tall building known as the Commonwealth Advisory Aeronautical Research Council (CAARC) model, after Melbourne (1980) and investigated flow patterns, mean and root-mean-square (*rms*) pressure coefficients on the building perimeter.

With other buildings present in close proximity, the dynamics of the wind flow becomes much more complex and flow interference occurs (Khanduri *et al.* 1998). Most of the numerical studies for assessment and evaluation of interference effects has been limited to the use of Reynolds-averaged Navier-Stokes (RANS) equations (Zhang and Gu 2008, Lam and To 2006). For a numerical model to be successful, similar efforts taken in their boundary-layer wind-tunnel counterpart to produce proper inflow characteristic is necessary. In this study, numerical simulation, a systematic investigation of the effects of various inflow turbulence generations for Large-Eddy Simulation (LES), is presented. LES for the CAARC model has been carried out both for with and without adjacent building test configurations. A detailed validation done through a comparison with wind tunnel data obtained by RWDI USA LLC, (Miramar Florida) (Dagnew *et al.* 2009, Dagnew and Bitsuamlak 2010) is also presented.

2. Inflow turbulence generation

The application of LES for estimating time-history of dynamic wind loads requires transient inlet boundary conditions and heavily depends on the generation of accurate inflow turbulence at the inlet boundary. Inlet boundary conditions of LES simulations, of high Reynolds number turbulent flow, should possess accurate representation of oncoming inflow turbulence, satisfying prescribed spatial and temporal correlations (Tamura 2008, Dagnew and Bitsuamlak 2013). In bluff body aerodynamics, the grid spacing is mostly too coarse to resolve any large component of the turbulent spectrum. This coarse spacing is most pronounced near the inlet boundary, where few grid cells are allocated in order to reduce computational cost. Conversely, the majority of cells are clustered in the near-wall region to resolve boundary layers, flow separation and reattachment, and wake and re-circulating regions. However, the purpose of the inlet boundary condition is to supply scales relevant to the grid, i.e., ensuring the inlet turbulence have integral length and time scales related to the grid size (Δx , Δy , Δz), and the computational time step Δt .

There are several techniques to generate turbulence fluctuations. A comprehensive review by Tabor and Baba-Ahmadi (2009) and Huang *et al.* (2010) discussed various methods commonly used for generation of inflow turbulence at the inlet boundary of LES simulations. These methods include recycling methods, precursor databases, and synthetic turbulence methods. The present study investigated the suitability of these methods for LES-based wind load evaluation of tall buildings. To perform this study suitably, an experimental ABL wind flow simulation has been conducted and flow statistics have been measured.

2.1 Experimental ABL wind flow simulation

A practical approach for obtaining the inlet boundary flow variables for CFD simulations is to generate a time history of wind velocities through empty BLWT measurements (Fig. 1(a)). Then, flow statistics of the time-history for the standard profiles such as open, suburban, and urban profiles can be used in the numerical method to accurately prescribe the inlet boundary of the LES simulation. Once the flow statistics are generated, they can be used repeatedly by the LES model as required without the need to go back to the wind tunnel. In the present study, the wind tunnel ABL wind flow simulation has been conducted at the RWDI USA LLC testing facility. Inflow data with a record length of 180 sec and a sampling frequency of 515 Hz has been collected at the RWDI boundary-layer wind tunnel (BLWT). An open type exposure with "power law exponent of 0.16" was obtained from the ABL experimental simulation (Fig. 1(b)). Statistics of fluctuating turbulence such as length-scale and turbulence intensities are then obtained from the time history of the velocity data measured in the BLWT that were subsequently used by the various inflow turbulence generators. Table 1 summarizes the turbulence characteristics of the simulated ABL wind flow.

Table 1 Measured inflow wind characteristics of rural terrain

Level	Elevation(m)	Mean velocity $U(m/s)$	Turbulent intensity (%)			Integral length (m)		
			I_x	I_y	I_z	${}^xL$	${}^yL$	${}^zL$
1	0.1524	10.381	24.00	7.30	16.30	0.480	0.090	0.160
2	0.3048	11.458	22.50	8.90	14.80	0.540	0.145	0.175
3	0.4572	12.061	21.00	10.30	14.50	0.550	0.160	0.192
4	0.6096	12.810	19.60	11.00	13.90	0.600	0.175	0.200
5	0.9144	13.647	16.90	10.20	12.40	0.630	0.185	0.205
6	1.2192	14.438	15.60	9.30	11.30	0.640	0.190	0.210
7	1.5240	14.995	12.80	6.90	9.30	0.650	0.125	0.191

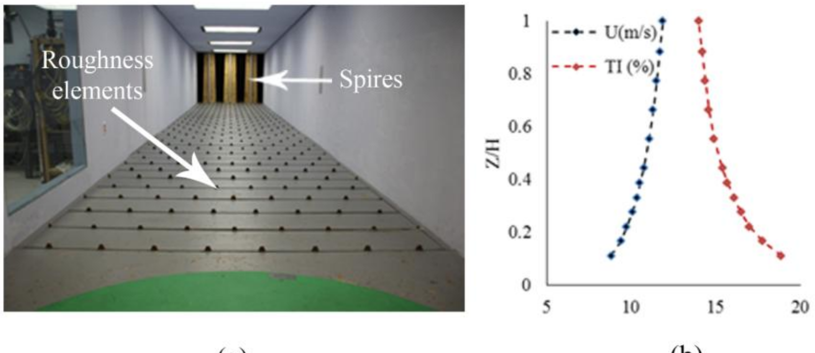

(a) (b)

Fig. 1 (a) An empty wind tunnel set up for ABL testing at RWDI Miramar, FL; and (b) Measured mean wind velocity and turbulence intensity (TI)

2.2 Numerical generation of inflow turbulence for LES simulation

2.2.1 Recycling method

The recycling method is based on Lund *et al.* (1998) proposal where the computational domain is subdivided into two domains. This method can be implemented in two different ways. One method involves using an auxiliary simulation in which an empty computational domain simulation is done and the turbulence data is stored for a subsequent simulation (Fig. 2(a)). Once the simulation is run enough number of flow-through times, i.e., the flow statistics are stable, a plane of data will be extracted and stored for a later use by the main simulation. The other method is by a combined domain approach, where the domain upstream of the calculation domain, also called "driver domain", is used to generate spatially developing boundary layer flow by re-scaling instantaneous velocity at a plane, also called the recycling plane, and remapping the flow back to the inlet boundary (Fig. 2(b)). The "calculation domain" will use the plane of data generated on the fly by the "driver domain". Kataoka and Mizuno (2002) later simplified using Lund's method by assuming that the growth of the inner boundary layer thickness is insignificant within the computational domain. Hence, instead of recycling the whole value of the instantaneous velocity components, only the fluctuating components will be recycled. In this method, the velocity components at the inlet boundary are defined as follows

$$\begin{aligned} u_{inlet}(y,z,t) &= \langle u\rangle_{inlet}(z) + \phi(\theta)\times\{u(y,z,t) - \langle u\rangle(y,z)\}_{recy} \\ v_{inlet}(y,z,t) &= \phi(\theta)\times\{v(y,z,t) - \langle v\rangle(y,z)\}_{recy} \\ w_{inlet}(y,z,t) &= \phi(\theta)\times\{w(y,z,t) - \langle w\rangle(y,z)\}_{recy} \end{aligned} \tag{1}$$

where subscripts $\langle . \rangle$ denote the time-averaged value in the span-wise direction and $\langle u\rangle_{inlet}$ is the prescribed mean velocity profile. The damping function, $\phi(\theta)$, prevents development of turbulence in the free stream and is given by

$$\phi(\theta) = \frac{1}{2}\left\{1 - \frac{tahn\left[8.0(1-\theta)/(-0.4(\theta-0.3)+0.7)\right]}{tanh(8.0)}\right\} \tag{2}$$

where $\theta = z/z_G$, and z and z_G are the height and gradient height, respectively.

In this paper, one study case was to investigate the modified Lund's recycling method (Kataoka and Mizuno 2002). Inhomogeneous perturbations generated by the Weighted Amplitude Wave Superposition (WAWS) technique were added to the inlet boundary (Swaddiwudhipong *et al.* 2007). The WAWS method is based on Shinozuka (1985), where a fluctuating velocity field is generated from samples of a single random Gaussian process with zero mean and prescribed model energy spectral.

$$u'(t) = \sqrt{2}\sum_{k=1}^{N}\sqrt{S_u(f_k)\Delta f}\cos(2\pi f_k t + \varphi_k) \tag{3}$$

where $S_u(f_k)$ is the one-sided von Karma spectral model of $u'(t)$, f_k are the central frequencies of the interval Δf, and φ_k is the random phase angle uniformly distributed from 0

to 2π . For the present study, the energy spectrum of fluctuating velocities is described by the von Karman model spectrum (Simiu and Scanlan 1996).

2.2.2 Synthesized turbulence

A synthesized turbulence fluctuations generation technique is based on the method of Kraichnan (1970). In this method, an arbitrary energy spectrum is used to prescribe the amplitude of velocity fluctuation as a function of a wave-number.

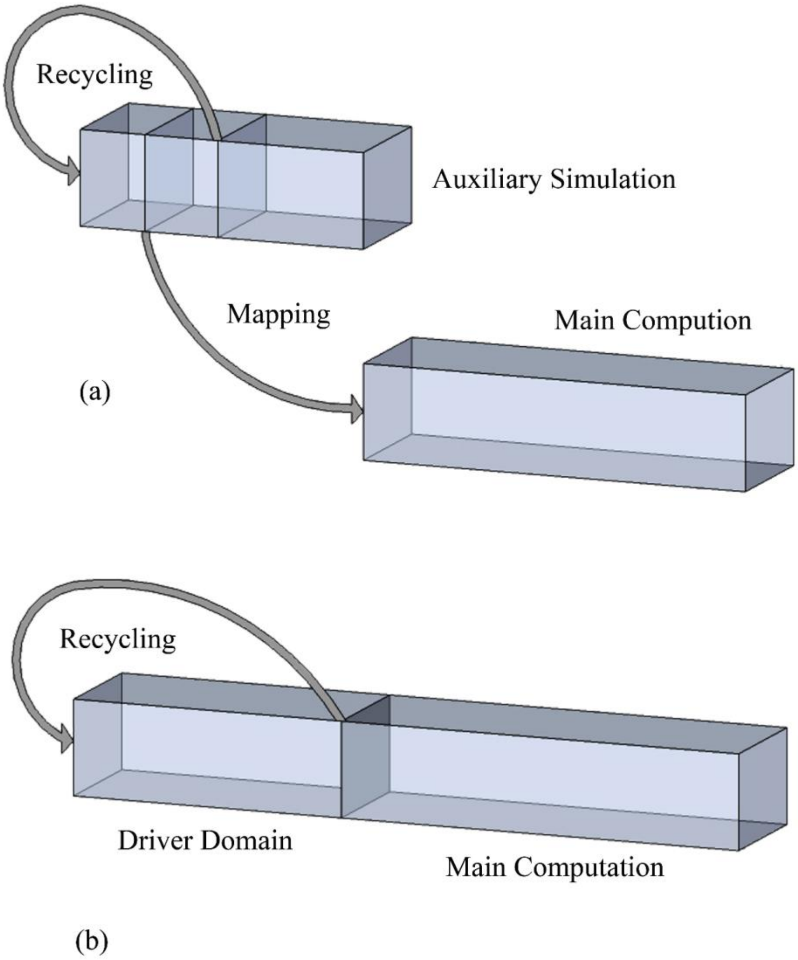

Fig. 2 Implementation of Lund's recycling method: where (a) auxiliary pre-computation is mined to produce velocity inlet data and (b) computational domain is subdivided into driver and main computation domain

2.2.2.1 Inhomogeneous random flow generation

Smirnov *et al.* (2001) modified Kraichan's method by incorporating turbulence length- and time –scales. These modifications ensured the generation of divergence-free isotropic fluctuations. A brief presentation of the random flow generation technique is given as follows

$$u_i(\tilde{x},t) = \sqrt{\frac{2}{N}}\sum_{n=1}^{N}[p_i^n \cos(\tilde{k}_j^n \tilde{x}_j + \omega_n \tilde{t}) + q_i^n \sin(\tilde{k}_j^n \tilde{x}_j + \omega_n \tilde{t})] \tag{4}$$

where $\tilde{x}_j$, $\tilde{t}$ are the scaling parameters for the length- and time-scale of turbulence and $\tilde{k}_j^n$ ω_n are sample of wave number vectors and frequencies of the modeled turbulence spectrum, respectively. The Gaussian model spectrum employed in this method is expressed as

$$E(k) = 16(2/\pi)^{1/2} k^4 \exp(-2k^2) \tag{5}$$

The spectrum model is mainly designed to represent large energy-carrying structures and thus undermine eddies within the inertial sub-ranges. However, turbulent ABL flows have demonstrated a cascade of energy between turbulent eddies. In such a flow, the inertial sub-range plays a vital role in transferring energy from a large-energy containing range to small-scale eddies of the dissipation range. The small-scale eddies in the dissipation range are in the same order of Kolmogorov scale (η) and the energy will eventually be converted to internal energy and dissipate. Considering the modeling principles of LES, i.e., resolving the flow up to the filtering (grid size) and modeling small-scales, the length-scale of inertial sub-range lies between the integral length scale and Kolmogorov scale and their contribution is very significant. For example, the ANSYS Fluent 13 package has implemented this technique as a Spectral Synthesizer for generation of inflow turbulence at the inlet boundary of unsteady simulations. Hence, for computational wind engineering applications, such as the wind effect on structures submerged in the ABL layer, the inflow fluctuations should be representative of a realistic turbulence spectrum such as the von Karman spectrum model. In the work of Huang *et al.* (2010), further modification of Kraichnan's method was done to generate a flow field that can satisfy any given arbitrary spectrum. The technique (also called DSRFG) uses discretization of arbitrary 3D spectrum and synthesized fluctuation to generate spatially correlated turbulent flow field. For illustrative purposes, we have used the Spectral Synthesizer technique and investigated its effects on wind load evaluation.

2.2.2.2 Homogenous random flow generation

Davidson (2007) and Senthooran *et al.* (2004) employed a synthesized turbulent inlet boundary for hybrid LES-RANS and RANS simulation, respectively. In the present study, the three-dimensional fluctuating velocity components were generated using the synthesized isotropic turbulent fluctuations method in addition to the Spectral synthesizer and recycling method already discussed. The random velocity field, which is defined as a finite sum of discrete Fourier modes, is given here for illustrative purposes

$$u_i'(x_j) = 2\sum_{n}^{N} \hat{u}^n \cos(k_j^n x_j + \psi^n)\sigma_i^n \tag{6}$$

where $\hat{u}^n, \psi^n$, and σ_i^n are the amplitude, phase and direction of the Fourier mode n, respectively. The notation used here follows that in (Billson *et al.* 2004, Davidson 2007). The wave-number vector k_j^n is chosen randomly on a sphere of radius, k_n . For an incompressible turbulent flow, $k_n . \sigma_n = 0$ where $n = 1, ..., N$. This relationship ensures isotropy of the generated velocity field. The wave-number vector $k_j{}^n$ and the spatial direction σ_n are thus perpendicular. The wavenumber vector $k_j{}^n$ is characterized by its spherical coordinates (k_n , θ_n , ϕ). The variables ψ_n , φ_n , α_n and θ_n were chosen randomly from their probability density functions. The amplitude $\hat{u}^n$ of each mode is computed from the three-dimensional model spectrum $E(k_n)$ in such a way that the isotropic fluctuations simulate the shape of the modified von Karman-Pao spectrum.

$$E(k_n) = \alpha \frac{2K}{3k_e} \frac{(k/k_e)^4}{[1+(k/k_e)^2]^{17/6}} \exp^{[-2(k/k_e)^2]} \tag{7}$$

The spectrum $E(k_n)$ is subdivided into *N* modes (typically 150-600), equally large.

$$\hat{u}^n = \sqrt{E(k_n)\Delta k}_{\,n} \tag{8}$$

where K is the turbulent kinetic energy and $k_\eta = \varepsilon^{1/3} \nu^{-3/4}$ is the Kolmogorov wave-number, ν is the molecular viscosity, and ε is the dissipation rate. Whereas α is a numerical constant which determines the kinetic energy of the spectrum and the wave-number k_e corresponds to the most energy containing eddies where $E(k_n)$ reaches maximum.

The fluctuating velocity fields generated by Eq. (6) are statistically independent of each other and thus have zero autocorrelation. Time correlation is created by using an asymmetric infinite time filter and a new fluctuation velocity field is computed at every time step.

$$(v')^m = a(v')^{m-1} + b(v')^m \tag{9}$$

where $a = \exp(-\Delta t / \tau)$, $b = (1-a^2)^{0.5}$ and m , Δt , τ denote the time step number, computational time step, and the turbulence time scale for which the autocorrelation function is reduced to $\exp(-1)$ respectively. This method offers a convenient way to prescribe turbulent length- and time- scales independently (Billson *et al*. 2004). For the present study, the length- and time- scales measured from BLWT were used.

3. Outline of BLWT experiment and LES simulation for wind load evaluation

3.1 High frequency pressure integration (HFPI) technique

The HFPI method is based on the simultaneous measurement of pressures at several locations on a building surface. The pressure taps were installed at a fine enough resolution over the building surfaces. The study (CAARC) building had a rectangular prismatic shape with dimensions 30.48 m (x) by 45.72 m (z) by 182.88 m (y) height. The BLWT HFPI model was instrumented with 280 pressure taps. Time histories of pressures were measured and stored for post-test analysis. The design wind loads were calculated by integrating the instantaneous pressure over the corresponding contributory area. The geometrical modeling and pressure tap distribution adopted for the LES simulation mimics the BLWT-HFPI model. All the experiments have been carried out at 1:400 scale. The individual pressure time histories were used to form time series of the base loads, from which wind load statistics and spectra were obtained. Figs. 3(a) and 3(b) show the pressure tap layout for the BLWT-HFPI model and the corresponding CFD setup, respectively along with the overall equivalent full-scale dimensions, direction notations, and wind flow angle. The wind flow is described in a Cartesian coordinate system (x, y, z), in which the x-axis is aligned with the stream wise flow direction, the z-axis is in the lateral direction and the y-axis is in the vertical direction.

3.2 Study cases for the LES simulation

In the present study, three building configurations have been investigated (Fig. 4). Case 1 presents the isolated CAARC building model under various inflow turbulences. Cases 2 and 3 simulate scenarios where half and full-height adjacent buildings are situated upwind of the CAARC model, respectively. Table 2 summarizes LES cases considered, along with the wind angle of attack, and mesh resolution adopted.

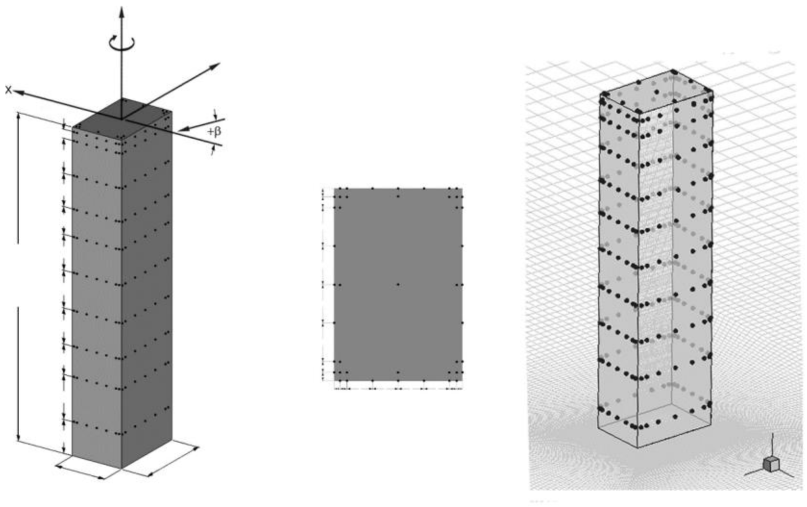

Fig. 3 CAARC building model: Dimension and pressure tap locations (a) and (b) BLWT, (c) CFD

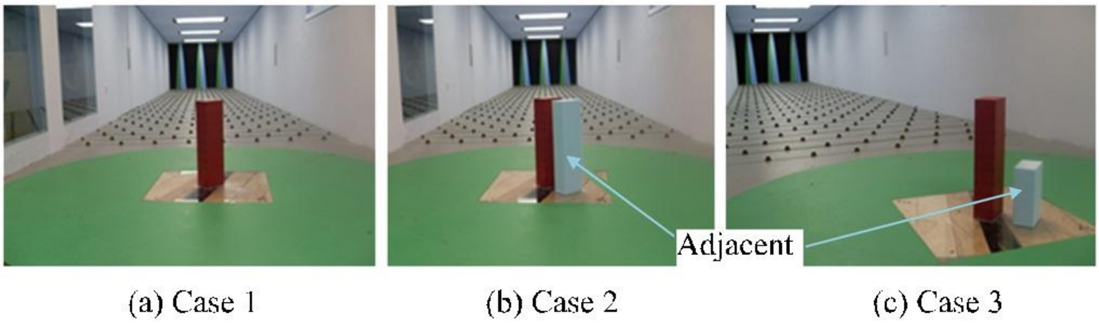

(a) Case 1 (b) Case 2 (c) Case 3

Fig. 4 Experimental load evaluation test configurations: Isolated CAARC model (a) and with adjacent (b) full-height, and (c) half-height building

Table 2 LES cases

Case	Configuration	Wind angle of attack	y+
Case 1	Isolated	0^0	1 < y+ < 5
Case 2	Half height adj. bldg. upwind of CAARC	0^0	1 < y+ < 5
Case 3	Full height adj. bldg. upwind of CAARC	0^0	1 < y+ < 5

3.3 Computational domain and boundary conditions

The computational domain (CD) defines the region where the flow field is computed. It should be large enough to accommodate all relevant flow features that could potentially alter the characteristics of the wind flow field (Franke 2006, COST 2007, AIJ 2008- Tamura *et al*. 2008). The CD for Case 1 was extended to $8D_z$ (D_z is width of the CAARC building model) upwind of the model building and to $25D_z$ downstream of the target building. Laterally, the CD spanned $8D_z$ away from the side surfaces of the building model and the top boundary was placed at $2.5H$ (H is the model building height). Fig. 5 illustrates the computational domain and boundary conditions used for Case 1. The blockage ratio, or the ratio of the wind-ward face of the CAARC model to the inlet plane, was about 2%, which is less than 5% of the ratio as recommended by COST (2007). Boundary conditions define the surroundings that have been cut off by the CD and idealize the influence of the actual flow environment under consideration. These conditions significantly affect the accuracy of the CFD prediction. At the inlet boundary, the mean wind velocity profile, as measured in the wind tunnel testing, was determined from the law-of-the-wall. For the ground and building surfaces, no-slip wall boundary conditions have been assumed. A symmetry boundary condition is employed at the top and lateral surfaces. Since details of the flow variables for all 3 cases were not known, the following accommodations had to be made. For Case 1, an outflow boundary was applied at the outlet plane while for Cases 2 and 3, the upwind CD was increased by $2D_z$, upstream neighboring building but the boundary conditions remained the same. The separation (S) between the buildings, based on the wind-ward width (B), was kept at S / B=0.67.

Computational grid, spatial, and temporal discretization schemes

The Reynolds number based on building height H and the measured roof top velocity U_H, measured at 1.22 m upwind of the test building, was $3x10^5$. Hence, the boundary layer regions required a high-resolution mesh clustered near the building surfaces. O-grid hexahedral meshes were generated by using the technique of blocking in ANSYS ICEM CFD mesher (ANSYS ICEM CFD user manual, 2011). In the inner sub-layer region, the boundary layer meshes were inflated from the wall surface and the first cell was placed at a distance of y_p = 0.0001 with a stretching ratio of 1.05. Such a position ensured that y^+ was less than 5 units and minimized the cut-off error of the wave-number in the LES modeling (Murakami 1998). In addition, the computational domain was subdivided into multiple parts to have better control and distribution of the computational grid points around the model building and wall boundary (See Fig. 6). For the target building, the O-grid meshing, which covers a region of $5D_z \times 5D_z$, was generated using 80 grid cells and the geometrical edge meshing law. The grids were clustered near the building with a stretching ratio of 1.05, and there were 52 grid points uniformly distributed in the lateral direction. In the lateral direction, outside of the $5D_z \times 5D_z$ region, 26 grid points with an initial spacing of 0.057 and a stretching ratio of 1.075 were used. In the x-direction (stream-wise), 40 grid points were used and the first grid point was placed at 0.01m with a stretching ratio of 1.041 from the building bounding box to the inlet plane, which spans $8D_z$. For the downstream domain starting from the end of the o-grid bounding box ($5D_z \times 5D_z$) to the outflow boundary, 60 grid points at a spacing of 0.01(with stretching ratio of 1.041) were used. Vertically, 158 grids points with y_p = 0.0001 were distributed while the grid points were clustered near the ground surface and the top surface of the building model (with stretching ratio of 1.0+5). For Case 1, a total of 4,782,784 3D computational grid cells were used. For Cases 2 and 3, the same mesh generation technique was adopted. A total of 6,913,565 and 6,913,562 hexahedral cells were used for Cases 2 and 3, respectively.

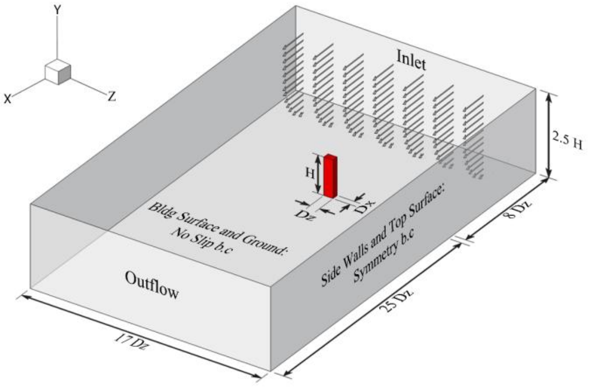

Fig. 5 Computational domain and boundary conditions for Case 1

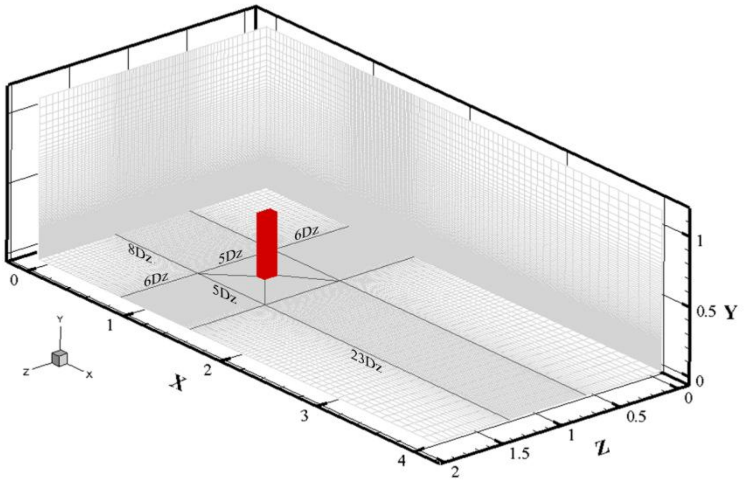

Fig. 6 Arrangement of computational grids

3.5 Turbulence modeling and numerical schemes

3.5.1 The LES model

LES is a multi-scale computational modeling approach that offers a more comprehensive way of capturing unsteady flows. The use of LES as a wind load evaluation tool has been significantly improved in recent years through the following numerical techniques (a) numerical generation of transient inflow turbulence (Kraichan 1970, Lund *et al*. 1998, Nozawa and Tamura 2002, 2003, Smirnov *et al*. 2001, Batten *et al*. 2004), (b) development of efficient sub-grid scale turbulence modeling techniques suitable for unsteady three-dimensional boundary separated flows, and (c) numerical discretization with conservation of physical quantities for modeling complicated geometry (Tamura *et al*. 2008). Because of these advancements, LES holds promise to become the future method for computational wind engineering (CWE) modeling for which turbulent flow is of pivotal importance (Tamura 2008, Tucker and Lardeau 2009, Sagaut and Deck 2009). In the present study, the Dynamic Smagornisky-Lilly subgrid-scale (SGS) model based on Germano *et al*. (1996) and Lilly (1992) have been employed. In this method, the Smagornisky constant, C_s, is computed dynamically according to the resolved scales of motion.

3.5.2 Adopted numerical schemes for LES

For discretization of convection terms, central-differencing based schemes give the least numerical diffusion and the best accuracy compared to the upwind schemes, as demonstrated by Martinuzzi and Tropea (1993). However, for high *Re* flows in the wake region, such as the present cases, this scheme can become unstable, giving unphysical oscillations (‘wiggles’). The bounded-central-differencing (BCD) scheme, essentially based on the normalized variable diagram (NVD) approach (Leonard 1991) together with a convection boundedness criterion can detect and remove these wiggles in the wake region. As a result, the BCD scheme has been used for all the simulations in the present study. For temporal discretization, second-order schemes are advised for most computational wind engineering applications and have been used in the present study. A second-order scheme for pressure discretization has been applied. For pressure-velocity coupling, the Pressure Implicit with Splitting of Operators (PISO) algorithm with skewness and neighboring correction is recommended for the transient simulation and has been used in all LES simulation. PISO is based on the higher degree of the approximate relation between the corrections for pressure and velocity (ANSYS Inc. 2011).

The simulations have been carried out at the supercomputer center at Florida International University. The parallel computations have been carried out using 28 CPUs. A computational time step of $\Delta t = 5 \times 10^{-4}\ s$ with 5 sub-iterations, per time step, were used in all the simulations. Once the simulation ran for enough flow time and the solution statistics reached stable conditions, the time histories of the pressure and fluctuating velocities data were recorded for *2s* flow-time. Also, a strict convergence criterion of 10^{-5} has been applied to the residuals to ensure full convergence of the simulation.

4. Results and discussions

4.1 Assessment of numerically generated inflow turbulence

An auxiliary simulation is a common way of conducting numerical ABL wind flow simulations. Comparative studies of inflow turbulence generation methods have been carried out using auxiliary domain flow simulations. Three different inflow turbulence generation techniques have been investigated to assess their suitability for LES-based wind load evaluations. Table 3 summarizes the three cases considered in the parametric study.

Table 3 Comparative study of inflow turbulences

Inlet boundary	Turbulence generation method
Inflow-1	Spectral synthesizer method (Smirnov *et al.* 2001)
Inflow-2	Recycling method (Lund *et al.* 1998)
Inflow-3	Synthesized turbulence (using the method in Sec. 2.2)

Inflow-1 defines the inlet boundary based on Smirnov’s random flow generation algorithm, which is implemented in the commercial software, ANSYS FLUENT 13 solver, as Spectral Synthesizer method (ANSYS Inc. 2007). This method computes fluctuating velocity components by synthesizing a divergence-free velocity-vector field from the summation of Fourier harmonics. At the inlet and for the turbulence generator of Inflow- 1, the kinetic energy and dissipation rate is prescribed using $K = 3/2(IU_{avg})^2$ and $\varepsilon = 3/2(C_\mu k^{1.5})/l$, while the mean velocity profile is defined using Eq. (11). For Inflow-2, Lund’s recycling method and randomly generated fluctuations using the weighted amplitude wave superposition (WAWS) method were superimposed to the instantaneous velocity at the recycling plane of the auxiliary domain. Inflow-3 is based on random flow techniques, as described in Sec. 2.2. C code was developed based on these techniques and turbulence data was generated and stored for a subsequent simulation. Then, for every time step, the stored instantaneous velocity components were mapped to the inlet boundary of the main simulation. For all the three study cases, the statistical flow parameters (e.g., integral length, turbulence intensity (TI), and mean wind velocity) have been obtained from BLWT data (see Sec. 2.1). For all cases considered in the inflow turbulence investigation, the inlet boundary condition has been prescribed as

$$\begin{aligned}\bar{u}_i(y,z,t) &= U_{inlet}(y) + u'_{in}(y,z,t)\\ \bar{v}_i(y,z,t) &= V_{inlet}(y) + v'_{in}(y,z,t)\\ \bar{w}_i(y,z,t) &= W_{inlet}(y) + w'_i(y,z,t)\end{aligned} \tag{10}$$

where $U_{inlet}(y)$ is the mean wind velocity profile measured from the wind tunnel experiment. The mean velocities in the lateral and vertical directions have been set as $W_{inlet}(y) = V_{inlet}(y) = 0$ and the stream-wise velocity, $U_{inlet}(y)$ has been defined as follows based on data obtained from the wind tunnel experiment (Fig. 7)

$$\begin{aligned}&\langle u\rangle/u^* = y^+ && y^+ < 5\\ &\langle u\rangle/u^* = 2.5\ln(y^+) + 5.5 && 30 < y^+ < 500\\ &\langle u\rangle/u_H = (z/H)^{0.16} && y^+ > 500\end{aligned} \tag{11}$$

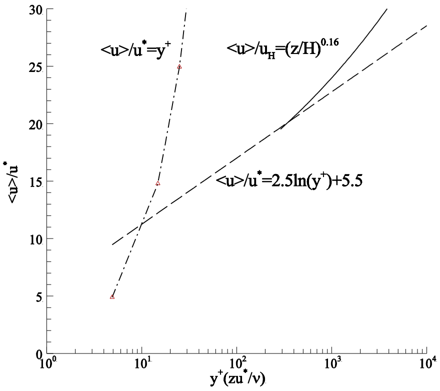

Fig. 7 Measured inlet velocity profile in semi-log scale

4.1.1 Application of the transient inflow turbulence method to LES

Time histories of velocity components were monitored at various points at the centerline of the incident plane during the LES of the auxiliary domain. Fig. 8 shows the samples of generated fluctuation in the stream-wise direction. The fluctuations were monitored in the upstream domain at the level of the model building height. The fluctuation generated by Inflow-1 and -2 showed poor spatial correlation compared to Inflow-3. The magnitude of the perturbation generated by Inflow-2 is very small. In cases where a large upwind computational domain is used, the fluctuation could dissipate before it reaches the incident plane and subsequently will affect the resulting wind load.

To further examine the performance of the numerically generated velocity fluctuation for the LES, the spectra of sample fluctuations monitored at the model building height (H) were compared with the von Karman model spectrum (Fig. 9). As pointed out in Section 3.3, the spectrum which results from Inflow-1 decays rapidly and follows the Gaussian spectrum model i.e., it only reproduces the large eddies and undermine eddies in the inertial sub-range. Compared to Inflow-1, Inflow-2 showed slight improvement in terms of reproducing eddies in the inertial sub-range but still not sufficient enough to represent a realistic wind field. When generating inflow turbulence for the LES simulation, the velocity fluctuations should be well reproduced at least up to $fH/U = 10$, since the velocity fluctuations in the inertial sub-range greatly affects the transfer of energy between eddies and the development and behavior of separated shear layers. The wind flow field generated using Inflow-3 satisfied this requirement.

Fig. 10 shows the two-point correlation of the vertical velocity simulated by the three turbulence generators. The normalized two-point spatial correlation is computed using $B_{ww}^{norm}(x,\hat{x}) = \overline{v'(x)v'(x+\hat{x})} \big/ v_{rms}(x)v_{rms}(x+\hat{x})$. Although the same number of computational grids and identical resolutions were used for all three Inflow conditions, the spatial correlation resulting from Inflow-1 and Inflow-2 decayed rapidly with separation distance $\hat{x}$, while for Inflow-3, the two-point correlation showed gradual decrease near the wall, which is an indication of strong spatial correlation (Davidson 2009). Fig. 11 illustrates the spatial representation of velocity fluctuations at the inlet boundary of the LES simulation from Inflow-1 and Inflow-3. As demonstrated by the figure, uncorrelated eddies were formed by Inflow-1 while realistic turbulence eddies with proper spatial correlation were generated by Inflow-3.

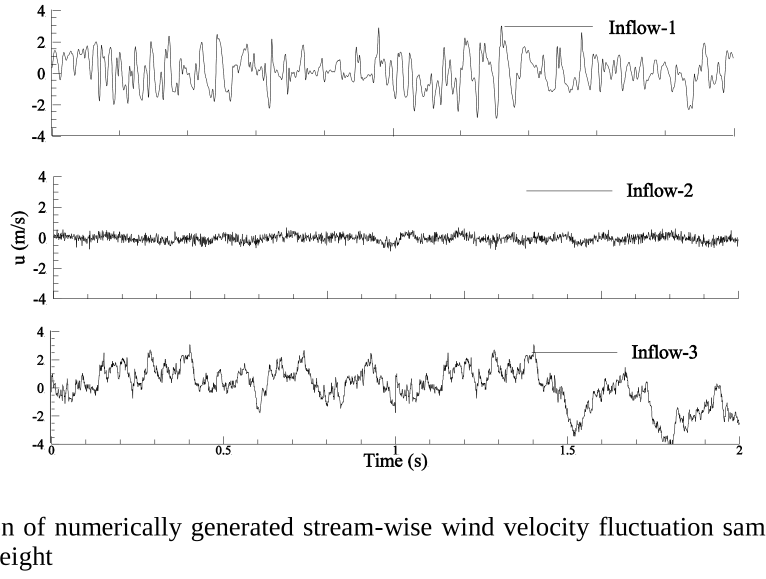

Fig. 8 Comparison of numerically generated stream-wise wind velocity fluctuation samples at the target building height

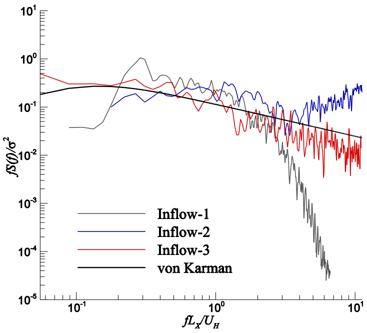

Fig. 9 Comparison of numerically simulated spectra with von Karman spectrum model at the model building height (L_U=0.55 m, and U_H=12.12 m/s)

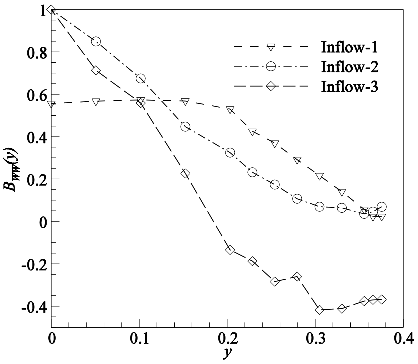

Fig. 10 Normalized two-point correlation of vertical velocity fluctuation

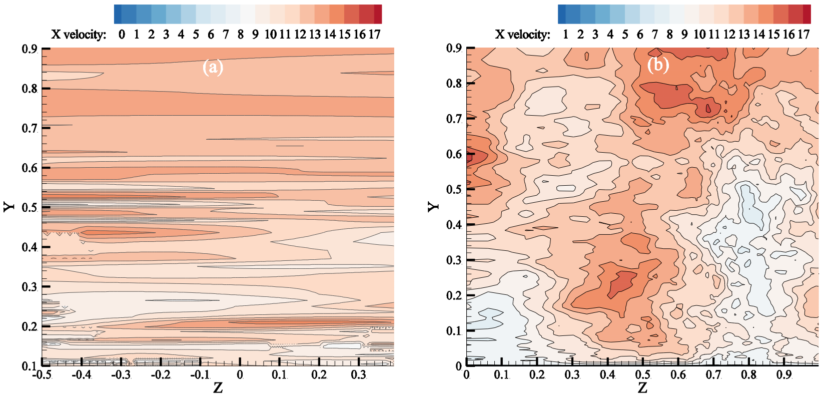

Fig. 11 Spatial representation of the stream-wise instantaneous velocity fluctuation at the inlet boundary: (a) Random flow generation method (Inflow-1), and (b) Synthetic inlet boundary (Inflow-3)

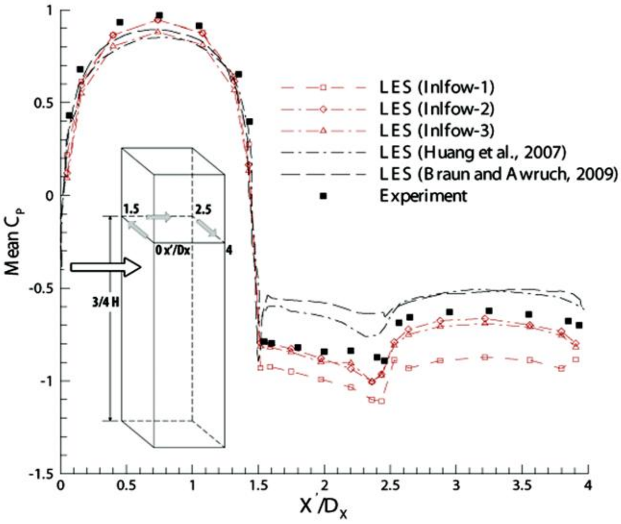

Fig. 12 Comparison of mean pressure coefficient at 2/3 H of CAARC model building

4.2 Mean wind pressure coefficient for isolated CAARC model

To gauge the prediction accuracy of LES for design wind loads evaluation and to assess the effects of oncoming inflow turbulence, a detailed study on the isolated CAARC building model (Case 1) has been carried out with various inlet boundaries. Fig. 12 depicts the comparison between numerically obtained mean-pressure coefficients with the BLWT data on the perimeter of the building measured at $2/3H$. The time-averaged non-dimensional pressure coefficients C_p was defined by

$$C_p = \frac{P - P_0}{\frac{1}{2}\rho U_H^{\ 2}} \tag{12}$$

where U_H is the reference velocity at the building height, H, $P - P_0$ is the dynamic pressure head, and ρ is the density of air. On the windward face, there is a very good agreement between the BLWT C_p values with those obtained from the present LES and those collected from the literature (Huang *et al.* 2007, Braun and Awruch 2009). On the side-walls, where flow separation occurred due to the sharp corner, the numerical results from Inflow-1 deviated from the BLWT measurements, especially at the trailing edge. LES with Inflow-1 also over-predicted the mean, C_p, on the leeward face. Inflow- 2 and Inflow- 3 showed very close agreement with the BLWT data on the side and leeward faces. The numerical data from literature under-predicted the pressure on the sidewall and leeward faces but these noticeable discrepancies could be due to differences in the boundary conditions in the literature as compared to the setup in this study. This comparison demonstrated how the incoming flow affected the predication accuracy, thus attesting to the necessity of prescribing appropriate incoming turbulence for unsteady simulations, such as LES.

Fig. 13 presents representative mean-pressure contour plots for wind-ward and lee-ward faces of Case 1. On the wind-ward face, the LES mean C_p contours estimated by the three inlet boundaries showed good agreement with the BLWT data. The mean C_p LES predictions for the leeward face showed marginal discrepancy with BLWT compared to the better agreement observed for wind-ward C_p values. Among the three inflow conditions, Inflow-3 performed marginally better than the predictions based on Inflows-1 and -2 conditions. Fig. 14 shows the root-mean-square (rms) of surface pressure coefficients. The rms produced by Inflow-3 on the wind-ward face, a place where the inflow fluctuation effect could be seen more apparently (compared to other faces which potentially experience more fluctuation due to flow separation) was in better agreement with the rms value from the BLWT. On the leeward face, the numerical result slightly deviated from the BLWT data.

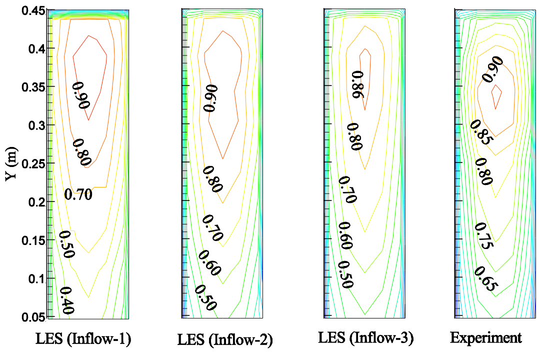

(a) Wind-ward face

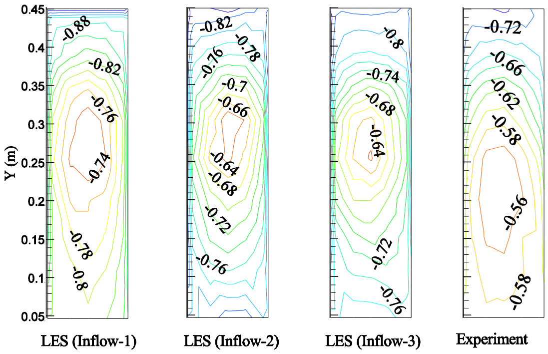

(b) Lee-ward face

Fig. 13 Mean pressure coefficient distribution over frontal and back faces of CAARC in a simulated ABL flow: Comparison between LES with various oncoming turbulence models and BLWT experiment

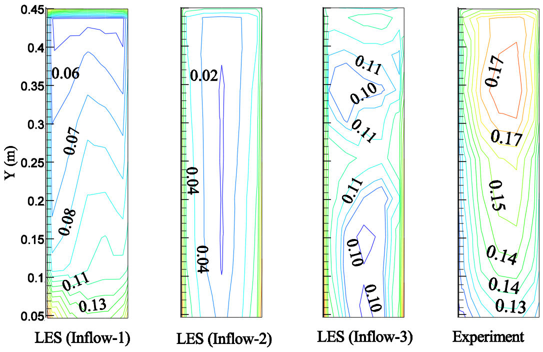

(a) Wind-ward face

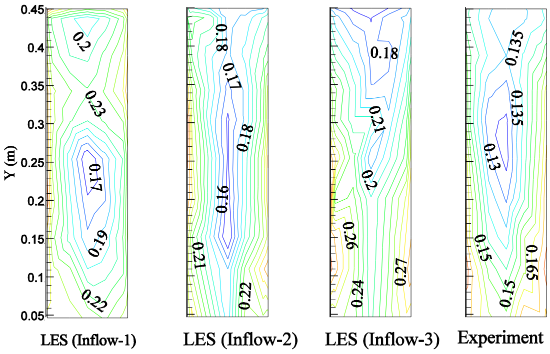

(b) Lee-ward face

Fig. 14 Distribution of fluctuating pressure coefficient (rms) over the frontal and lee-ward faces of CAARC in a simulated ABL flow filed: Comparison between LES with various oncoming turbulence models and BLWT experiment

4.3 Steady and fluctuating wind force coefficients for a single building

Following Obasaju (1992), the drag and lift coefficients, C_D and C_L, respectively are computed from the time history data of the LES simulation by considering the wind shear profile as follows

$$C_D = \frac{F_D}{(1/2\rho D_z \int_0^H U^2 dy)} \tag{13}$$

$$C_L = \frac{F_L}{(1/2\rho D_z \int_0^H U^2 dy)} \tag{14}$$

where F_D and F_L are the steady part of the along- and across-wind forces and become the same as F_X and F_Y when the angle of attack,α, equals 0°.

Using the stream-wise velocity profile measured in the BLWT, it can be shown that

$$\int_0^H U^2 dy \approx 0.781 U_H^2 H \tag{15}$$

Whereas the root-mean-square values of the fluctuating parts of F_X , F_Y , and torsional moment M are computed from the fluctuating components of the force time history as $C_{\sigma F_X} = \sigma_{F_X} /(1/2\rho U_H{}^2 D_Z H_{Level})$, $C_{\sigma F_Y} = \sigma_{F_Y} /(1/2\rho U_H{}^2 D_Z H_{Level})$, and $C_{\sigma M} = \sigma_{M_Y} /(1/2\rho U_H{}^2 D_Z{}^2 H_{Level})$, respectively. Here U_H is the mean wind velocity at the model building height H , and D_Z is the width in the wind-ward face.

Time-history of wind pressure coefficients on the 280 pressure taps strategically distributed on the surface of the model building (Fig. 3(b)) were recorded at each computational time step. At each level, 28 pressure taps and 7 taps per face, were placed. The drag and lift coefficients of Case 1 (for the three different inlet conditions) have been computed from the vector sum of tap forces (i.e., pressure measured at each tap multiplied by its tributary area) in the along- and across-wind directions, respectively. Fig. 15 presents the vertical distribution of the steady force coefficients calculated at each pressure tap level. There was good agreement between the LES and BLWT predictions of the steady force coefficients, especially LES with Inflow-3. Fig. 16 compares fluctuating rms force coefficients at each pressure tap level. The LES simulation demonstrated strong fluctuation on the along-wind direction when Inflow-3 was used.

Table 4 lists the comparison of the total experimental steady force coefficients (C_D , C_L , and C_M) and the rms force and torsional moment coefficients ($C_{\sigma F_X}$, $C_{\sigma F_Y}$, and $C_{\sigma M}$, respectively). In all three of the turbulence generation techniques considered, there was nearly 10% over-prediction of LES C_D compared to the experimental data. While the simulation from Inflow-1 and -2 under-predicted the lift force coefficient C_L , perturbation generated by Inflow-3 resulted in an improved C_L prediction compared to Inflow-1 and -2. For the rms coefficients, Inflow-3 showed much better performance, 15% over-prediction of $C_{\sigma F_X}$, less than 5% over-prediction of $C_{\sigma F_Y}$ and matching well for torsion moment compared to BLWT data (although the wind angle of attack considered for LES is not the critical one for torsion). The assumption of a homogenous flow field, one of the limitations of the present study, as applied in Inflow-3 could also have attributed to the over-prediction of the load coefficients. Fig. 17 illustrates the time histories of C_L and C_D , where the time-history of C_D showed small periodicity compared to C_L and strong fluctuation on the along-wind direction when Inflow-3 was used as the inlet boundary. Obasaju (1992) pointed out the need for longer averaging time in estimating C_D for high Reynolds number flow, as it changes irregularly. However, it was not computationally feasible to get statistics from CFD simulations for such long averaging times with most computational facilities such as those used in the present study. Hence, the over-estimation of the load coefficients by the CFD could be attributed to the short statistical averaging time (2 s) compared to the 180 s taken for the wind tunnel data. Overall the results from LES, especially from Inflow-3, were very encouraging.

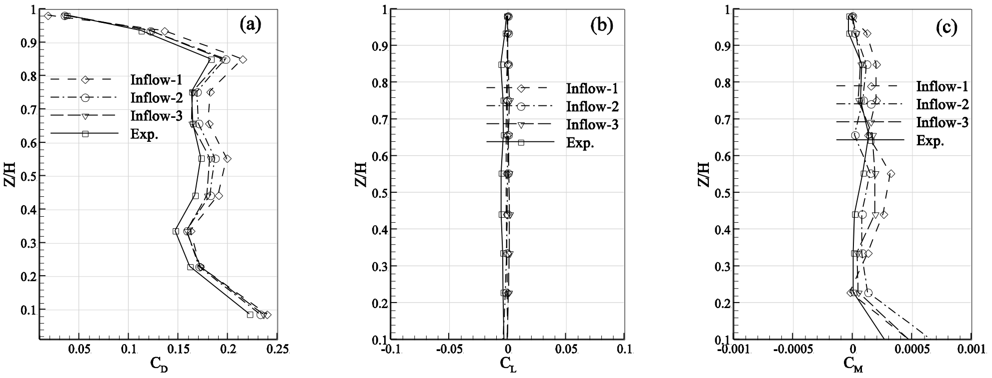

Fig. 15 Vertical distribution of mean (a) drag, (b) lift, and (c) torsional moment coefficients

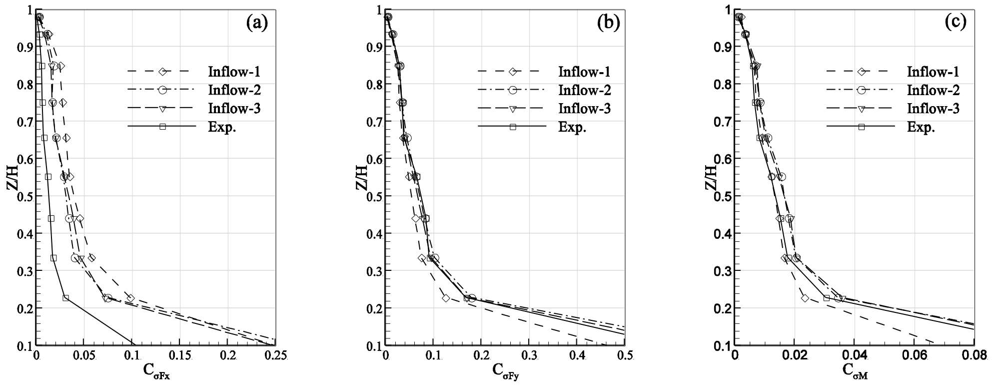

Fig. 16 Vertical distribution of fluctuating (a) drag, (b) lift, and (c) torsional moment coefficients

Table 4 Comparison of total steady and *rms* force coefficients

Inflow turbulence generation method	C_D	$C_{\sigma Fx}$	C_L	$C_{\sigma F_Y}$	C_M	$C_{\sigma M}$
Inflow-1	1.6957	0.6027	0.0042	0.9245	0.0019	0.1703
Inflow-2	1.6264	0.5453	0.0043	1.3209	0.0014	0.2456
Inflow-3	1.6091	1.2484	0.0100	1.2260	0.0013	0.2424
BLWT exp.	1.533	1.0737	0.0356	1.1818	0.0007	0.2150

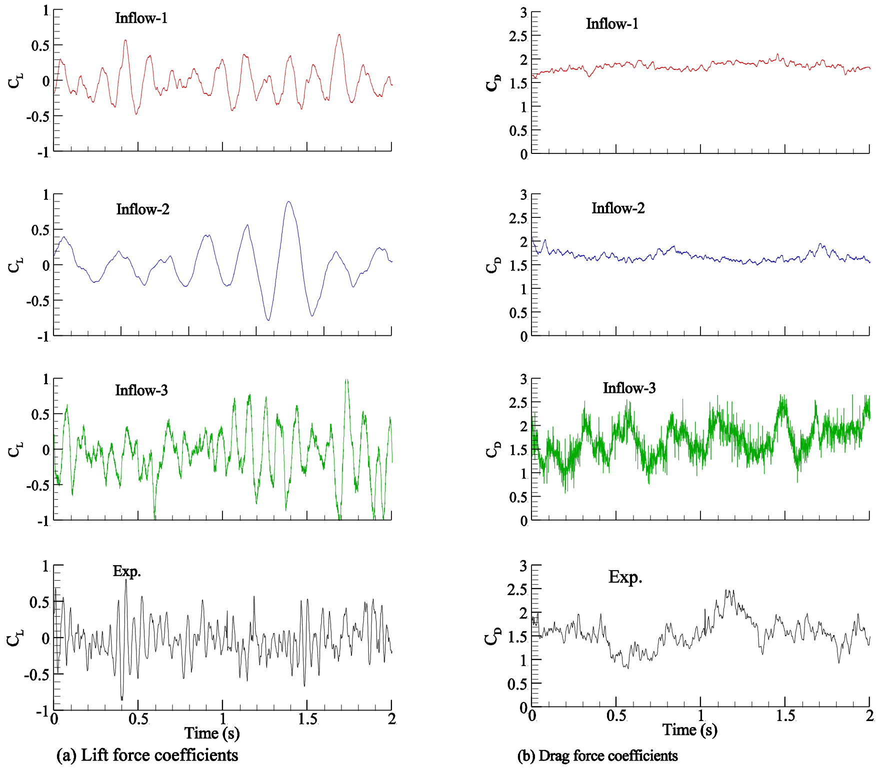

(a) Lift force coefficients (b) Drag force coefficients

Fig. 17 LES and BLWT time histories of C_L and C_D

4.4 Power spectra of the along- and across-wind loads for single building

The along- and across-wind force spectra obtained from the present LES simulation and the BLWT experiment are shown in Figs. 18 and 19, respectively. The spectra are presented in the form of $nS(n)/\sigma^2$ versus nD_z/U_H, where n is the frequency, $S(n)$ is the spectral density, and σ^2 is the variance. The forces at every pressure tap level were obtained by integrating the loads across the two opposite faces while the torsional moment was calculated by multiplying each tributary load with the corresponding lever arm from the geometric center of the model building. The total along-wind force spectrum predicted by Inflow-1 and Inflow-2 started decaying quickly within the frequency range of the inertial sub-range, which plays a vital role in transferring energy between large and small eddies for turbulent flow (Fig 18(a)). Higher frequency fluctuations were predicted by Inflow-3, which agreed well with the experimental data. This agreement is an indication that the synthesized turbulence method generated eddies within the inertial sub-range. Fig. 18(b) shows that the along-wind spectrum of the top tap level is in the region of flow separation. This observation gave some insight into how each method handled the separated turbulent flow. The total across-wind force spectra from the experimental results showed a sharp peak near the Strouhal number ($S = nD_z/U_H$), defined by using the roof-top velocity U_H, corresponding to the reduced frequency of $nD_z/U_H = 0.1$. This observation clearly suggests that strong and periodic organized Karman vortices were shed throughout the building height. The spectrum predicted by Inflow-1 and Inflow-2 showed a peak at a lower reduced frequency of $\approx 0.065$and spread to other frequencies. However, for Inflow-3 there was an improved prediction and the spectra peaked at the same reduced frequency of ≈ 0.1 as the wind tunnel prediction (Fig. 19(a)). To further validate the prediction accuracy of the numerical models, the wind force spectrum at the top pressure tap level, where strong flow separation occurred, is presented in Fig. 19(b). The power spectrum followed the same trend as the total wind force spectrum although it showed a broad peak and gradual decaying of eddies. The comparison of the total torsional moment spectra showed a typical peak around a Strouhal number of $nD_z/U_H = 0.1$, which is corresponding to the peak frequency range of the across-wind spectra (Fig. 20).

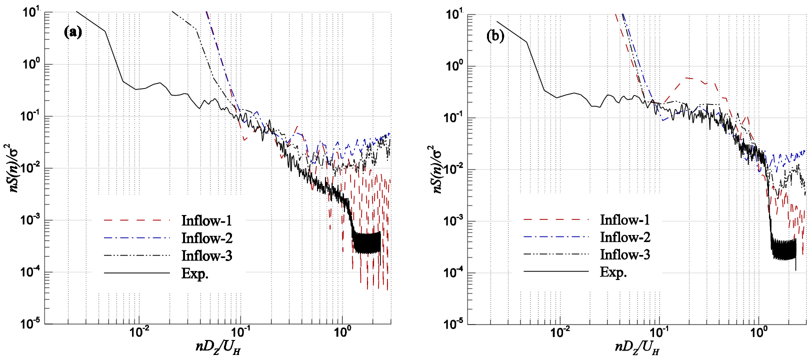

Fig. 18 Comparison of along-wind force spectrum spectra predicted by LES and BLWT: (a) total force, and (b) at the building model height (H=0.46)

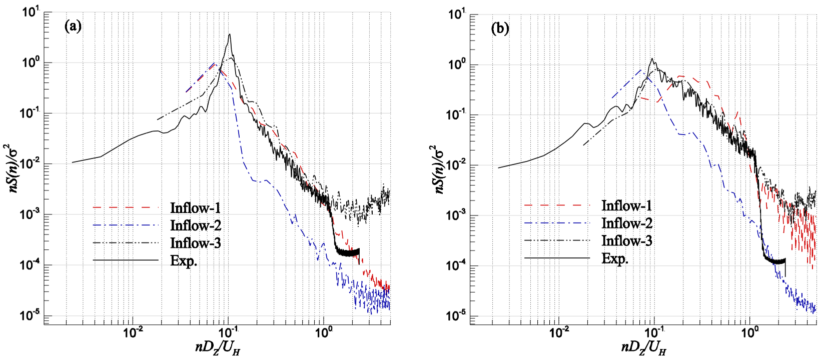

Fig. 19 Comparison of across-wind force spectrum spectra predicted by LES and BLWT: (a) total force, and (b) at the model building height (H=0.46)

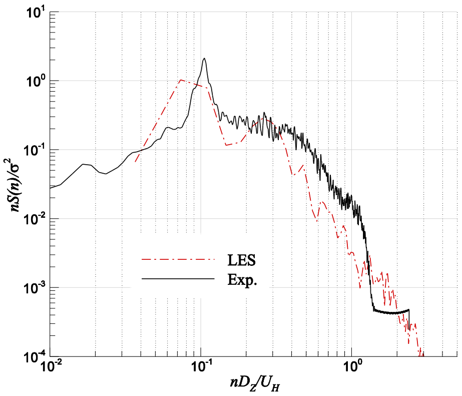

Fig. 20 Torsionalmoment spectrum (Inflow-3)

4.5 Flow field visualization of CAARC from various inflow turbulence

The time-averaged and instantaneous velocity flow field of the CAARC building model, taken at one instant of time, using various transient inlet boundaries is presented in Figs. 21 and 22, respectively. All of the basic flow features of the bluff body were captured by the LES simulations (Shah and Ferziger1997). The oncoming flow separates at the leading sharp corners (at the three corners of the wind-facing wall) and initiates a recirculation zone on the sidewalls and at the roof of the building, which are foot prints of the arch vortex in the downstream face, as illustrated in Figs. 21(a) to 21(f). The location of the arch vortex and the recirculation contraction zone in the wake region predicted by Inflow-1 and Inflow-2 are further downstream than the wake region predicted by Inflow-3. This difference might have contributed to the over-prediction of C_D , as well. The flow formed a recirculation zone above the roof and remained separated, as illustrated in the vertical sections plots of Figs. 21(b), 21(d), and 21(e). Fig. 22 illustrates the formation and shedding of asymmetric vortex at the trailing edge of the side faces and the wake zone. The streamlines of the instantaneous velocity revealed the complex and irregular nature of the wind-structure interaction flow field where the symmetric vortices are broken and formed by alternating asymmetric vortices. The flow field from Inflow-3 demonstrated a flow separation zone in the upstream face (Figs. 22(b), 22(d), and 22(f)). Strong, unsteadily moving vortices are formed by the synthetic inflow turbulence (Inflow-3) and they are responsible for better prediction of the lift-force coefficients, C_L and $C_{\sigma F_Y}$.

4.6 CAARC with an adjacent building

In experimental and computational wind loads on tall buildings, the more realistic scenario could be a configuration with adjacent buildings in vicinity of the study building. The presence of a neighboring building alters the aerodynamic characteristics of tall buildings and adds complexity to the flow for LES. As a part of ongoing research, the present study has attempted to assess these interference effects numerically. The configurations with an immediate adjacent building considered in the present study were listed in Table 2 and Fig. 4. Cases 2 and 3 represented the CAARC model with an upstream neighboring building with space separation (S), based on the wind-ward width (B) of the building whereas $S/B = 0.67$. The general settings of CAARC with adjacent building, such as boundary conditions and discretization schemes for both time and convection terms, were kept similar to Case 1. Table 5 lists the comparison between the LES and experimental force and torsional moment coefficients of the CAARC model building with an adjacent building situated on the upwind direction.

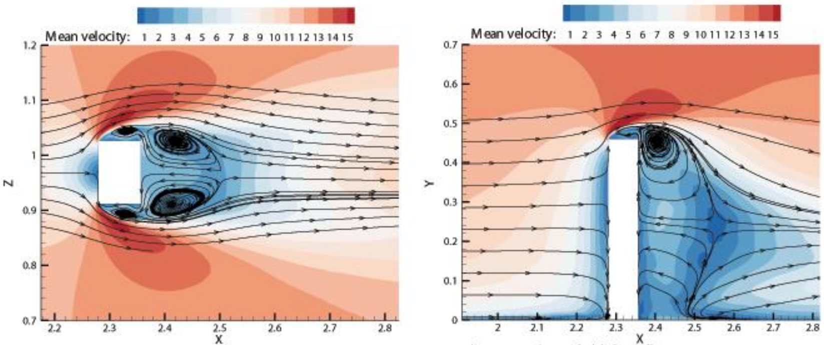

(a) Mean velocity field for Inflow-1 (b) Mean velocity field for Inflow-1

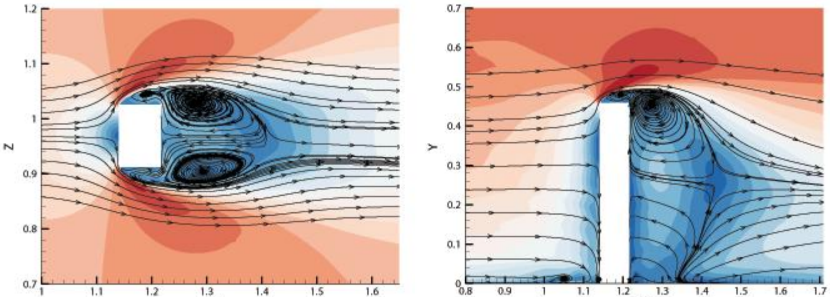

(c) Mean velocity field for Inflow-2 (d) Mean velocity for Inflow-2

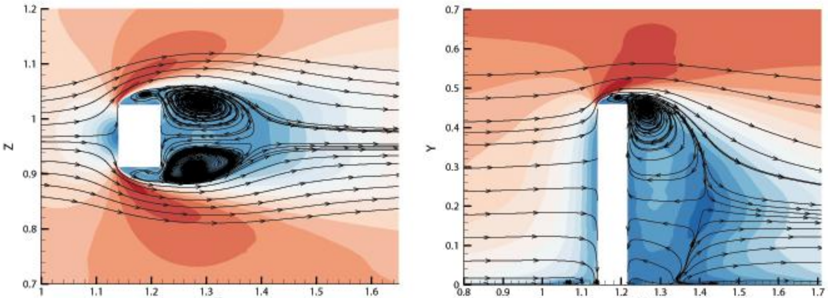

(e) Mean velocity field for Inflow-3 (f) Mean velocity field for Inflow-3

Fig. 21 Mean wind velocity contour and velocity streamlines: horizontal plane (Left), and a vertical section at centerline (Right)

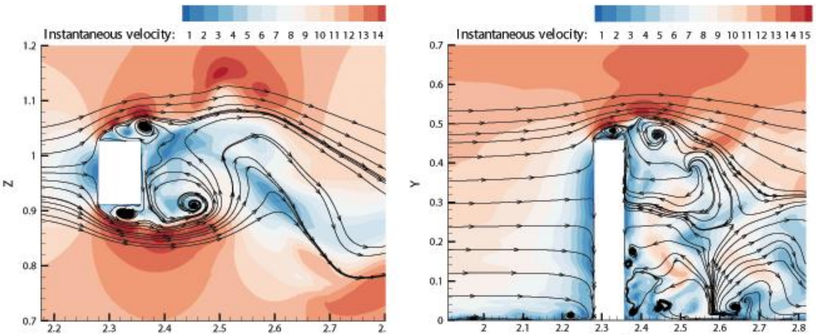

(a) Instantaneous velocity for Inflow-1 (b) Instantaneous velocity for Inflow-1

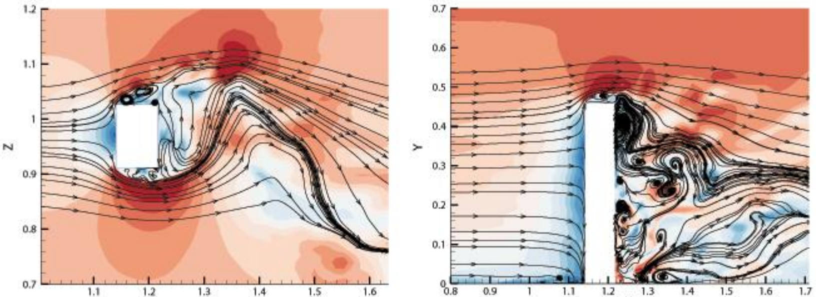

(c) Instantaneous velocity field for Inflow-2 (d) Instantaneous velocity for Inflow-2

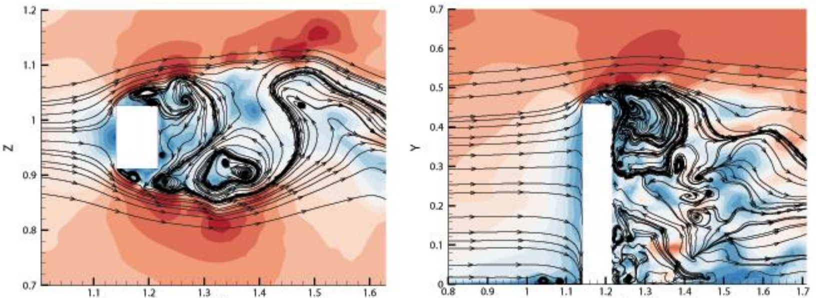

(e) Instantaneous velocity for Inflow-3 (f) Instantaneous velocity for Inflow-3

Fig. 22 Instantaneous wind velocity contour and velocity streamlines: horizontal plane (Left), and a vertical section on centerline (Right)

As expected, the adjacent building introduced a sheltering effect on CAARC that attributed to the reduction in the total along- and across-wind forces. For Case 2, the half-height adjacent building blocked the direct wind action up to H/2 and interfered with the flow around the rest of the building height. It is worth noting that the flow that separated at the adjacent building and then reattached to the study building (Fig. 23(a) and 23(c)). These combined phenomena and the narrow wake consequently reduced the drag- and lift-coefficients of the study building. Case 3 also displayed a very interesting phenomenon, in which the flow remained separated from the alternating Karman vortices of the side walls and sheds (Fig. 23(b) and 23(d)). As a result, a wider wake was created and the lift-coefficient of the study building increased significantly (Table 5). However, the flow reattached at the roof of the study building and reversed flow on the wind-ward face (Figs. 24 (b) and 24(d)). This phenomenon introduced strong suction on the wind-ward face of the study building, which resulted in a negative drag coefficient (Table 5a). However, for Case 2, the velocity increase from separation of flow at the roof of the adjacent building injected flow towards the windward face of the study building. The along-wind force in the flow direction also remained strong (Figs. 24(a) and 24(c)). The LES also performed well in predicting the torsional moment. Because of the symmetrical nature of the flow for the considered wind angle of attack, the torsional moment has been very small in all cases. The LES, averaged over two seconds of flow time, over-predicted the steady and fluctuating forces and moment. It also revealed very interesting flow details on how the flow field behaves when there is a neighboring building.

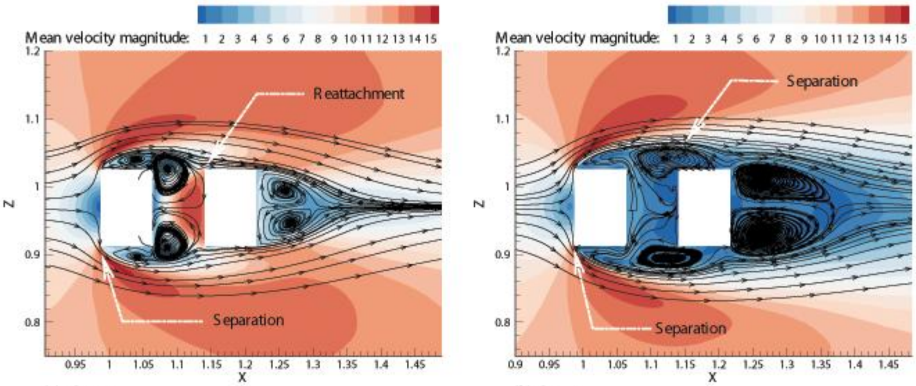

(a) Case 2 (b) Case 3

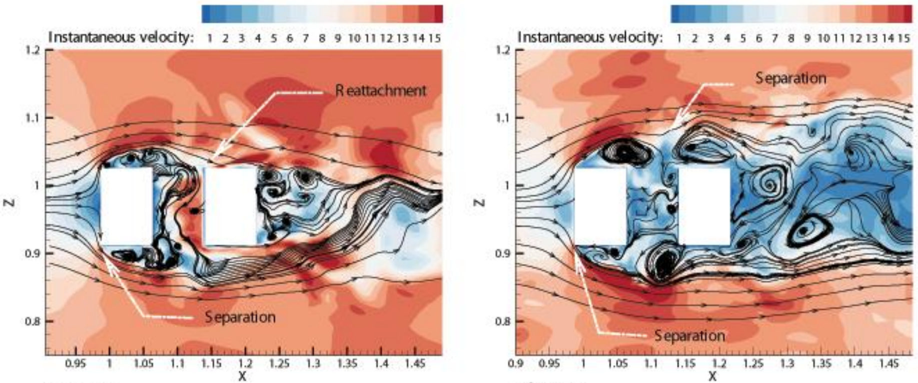

(c) Case 2 (d) Case 3

Fig. 23 Flow field of CAARC with an adjacent building: Mean velocity magnitude (top), and (bottom) instantaneous velocity on a horizontal plane at ($H / 3$)

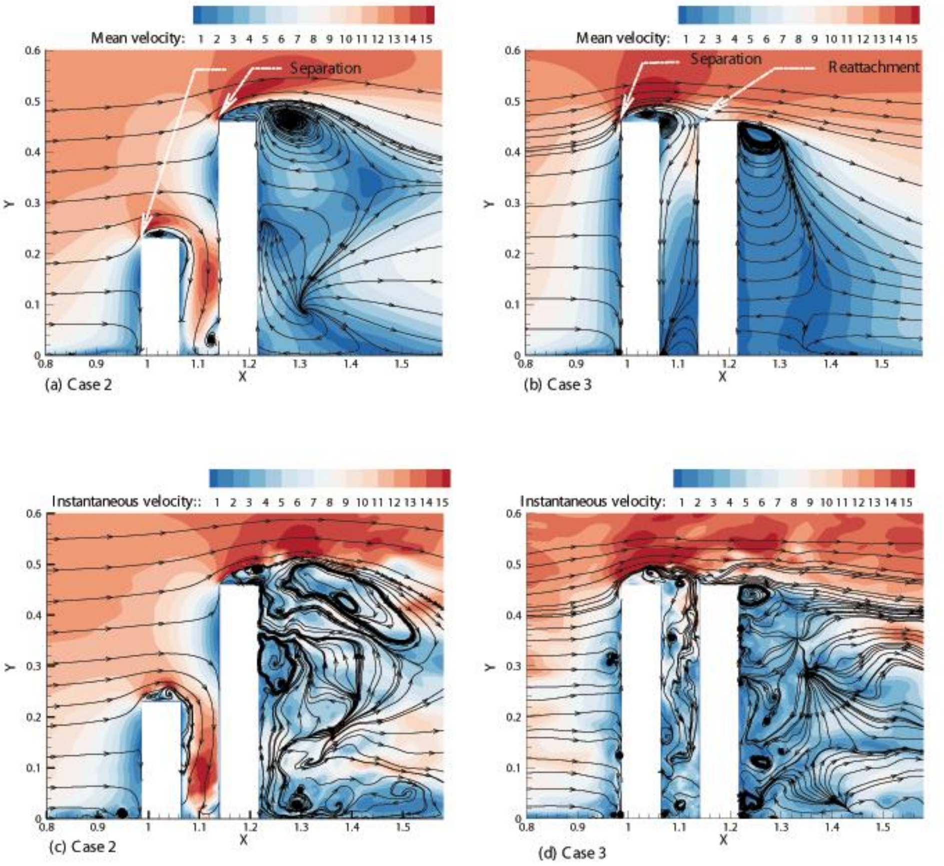

(a) Case 2 (b) Case 3

(c) Case 2 (d) Case 3

Fig. 24 Flow field of CAARC with an adjacent building: Mean velocity (top), and instantaneous velocity (bottom) at the vertical center plane

Table 5 Force coefficients: CAARC with adjacent building

Case	C_D		$C_{\sigma F_X}$		C_L		$C_{\sigma F_Y}$		C_M		$C_{\sigma M}$	
	LES	Exp.	LES	Exp.	LES	Exp.	LES	Exp.	LES	Exp.	LES	Exp.
Case 1	1.6091	1.533	1.2484	1.0737	0.0100	0.0354	1.2259	1.1818	0.0013	0.0007	0.2424	0.2149
Case 2	1.0250	0.8302	0.8420	0.5573	0.0120	0.0017	0.5794	0.5434	0.0002	0.0009	0.3402	0.1811
Case 3	-0.4760	-0.1709	0.6369	0.7687	0.0087	0.1006	0.6300	0.8644	0.0009	0.0035	0.2524	0.2458

In order to put error estimation in proper perspective, the percentile error was also estimated for drag, lift and torsional moment peaks. The peaks were estimated from the mean and rms values for each response. For comparison purposes, in the present case, a peak factor value of 3.5 was used based on an assumption that the global overall structural wind load follows a Gaussian distribution. Thus, the peak response can be estimated from the following equation

$$[Peak] = [Mean] + 3.5[rms] \tag{16}$$

The estimated errors in peak values for the isolated building were evaluated for the isolated building and for cases with a neighboring building. A maximum estimated error of 15% on peak drag for the isolated building case was obtained. The majority of the error was due to the r.m.s. estimation. The average error for the isolated building for all the base load cases was 5%. The estimation errors for the neighbouring building case were higher compared to the isolated building case. For case 2 where the small shorter building was upstream of the study building, the error on the lift for case 2 was only 7%. However the peak drag was from the LES was off by 30% compared with the experimental result, this is mainly due to the complex wake flow structure. To put this error in perspective it is good to note that the magnitude of the forces for a neighboring configuration are small compared to the isolated building case, thus the absolute errors are slightly smaller. For case 3 the higher error was observed for the peak lift due to the complexity of the flow resulting from the wake effects from the immediate large upstream building. The magnitude of the peak drag as well as the associated error of estimation was very nominal as the study building was fully sheltered by the tall upstream building.

In general, the error of estimation for study cases with immediate neighboring buildings are high compared to isolated cases. To improve these discrepancies in the future studies, the quality of the grid surrounding the neighboring buildings that causes the wake effects shall also be of high density. Allocating high density grids around the study building alone may not be sufficient for cases where the study building is located at the wake of an upstream building. In addition, there is a room for improvement by simulating a longer period and accounting for surface roughness effects both on the study building envelope and the ground surface between the upstream boundary and the study model and by using high grid resolution for the space between the upstream building causing the wake effects and the study building. Nevertheless, the overall agreement seems encouraging. From our personal experience in wind load estimation for tall buildings in a BLWT laboratory, errors on the order of 3% could be observed from a repeat test under similar conditions.

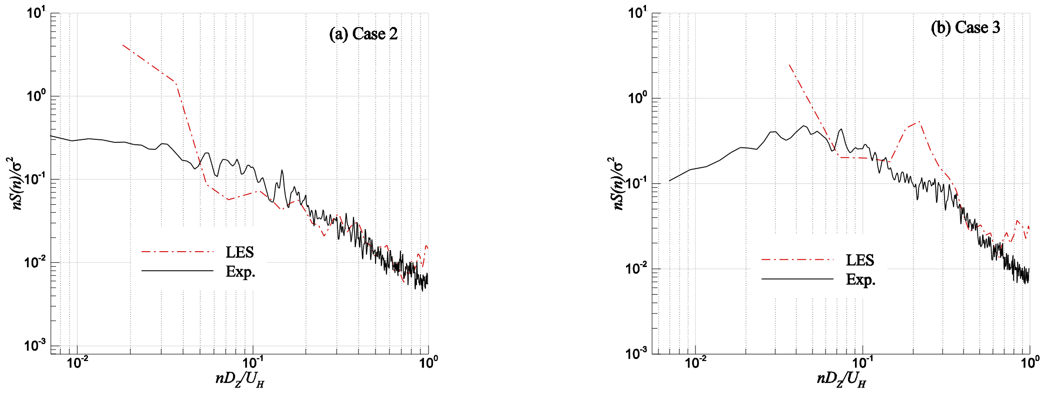

(a) (b)

Fig. 25 Along-wind force spectra for: (a) Case 2, and (b) Case 3

4.6.1 Spectral density

The total along-wind spectra of CAARC with an adjacent building are shown in Fig. 25. The LES spectrum of drag fluctuation of Case 2 agreed well with the experimental spectrum. However, the spectrum for Case 3 was slightly off. For the across-wind fluctuation spectra (Fig. 26, Case 2 shows a similar trend as the single building case spectra (Fig. 19(a)) except that there was slightly lower peak at the Strouhal number $nD_z/U_H = 0.1$ (Fig. 26(a)), which could be attributed to the sheltering effect of the neighboring building. Case 3 demonstrated flat across-wind spectrum without typical peak at the vortex shedding frequency. Overall, the numerical simulations reproduced the fluctuating force and captured eddies within the inertial sub-range.

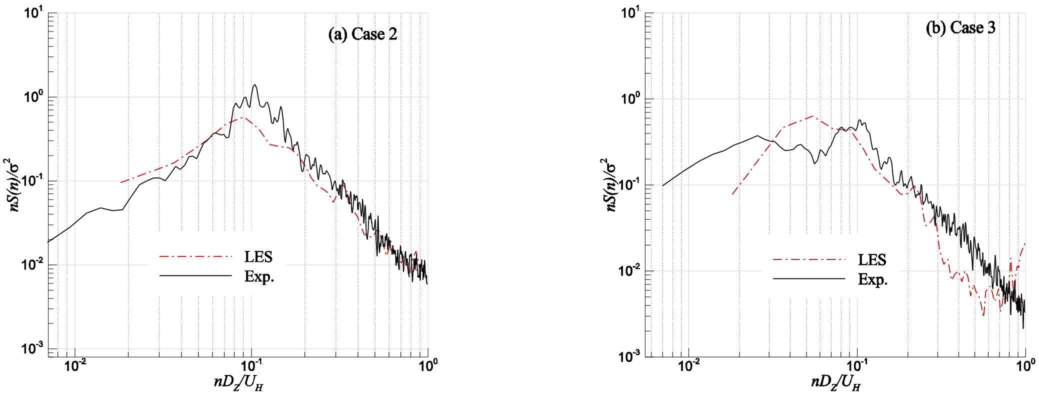

(a) (b)

Fig. 26 Across-wind force spectra for: (a) Case 2, and (b) Case 3

5. Conclusions

- Computational assessment of aerodynamic characteristics of a standard tall building (CAARC) with and without a neighboring building were performed and results were compared with BLWT data. The effects of inflow turbulence have been examined from the turbulence modeling principle of LES and computational wind load evaluation perspective.
- Three different inflow transient boundary conditions were investigated that utilized basic flow statistics (such as TI, wind speed, integral length scale) from the BLWT ABL data both using representative data for LES and for consistency reasons during the comparison. Inflow-3, that adopted fluctuation generated by using a synthetic method, showed better agreement with the BLWT data than the random flow generated by Smirnov's (also called 'Spectral synthesizer') and Lund's recycling methods. These results further attest to the need for proper inflow transient boundary conditions in agreement with suggestions by other CFD researchers. This is, in fact, analogous to the extreme care and effort that is taken during ABL flow simulation in the BLWT through use of upwind roughness elements, spires, or other types of active and passive flow controls. Similar care is expected from a numerical modeller.

- Generally, it can be concluded that LES with proper boundary conditions and enhanced computational resources, could prove useful for wind load applications. In the author’s opinion, the computational resource still is the bottle neck for full-fledged use of LES making it still expensive and more time consuming than standard BLWT wind load studies. One such limitation in the present study was perhaps the limited period of LES pressure time-history data generated than what might have been necessary to accurately predict the design wind force coefficients very similar to experimental method.
- The sheltering effects introduced by the neighboring building were fairly well captured by the numerical simulation when the adjacent buildings are placed upwind of the study building. Mean pressure coefficient increased for Case 2 when compared with the isolated CAARC model (Case 1).
- Sheltering effects and other complex interference mechanisms could be effectively explained owing to the continuous simulation capability of numerical simulations in space and time, thus leading to a better understanding of wind/structure interactions and the development of mitigation solutions that will lead to enhanced wind performance of buildings.
- High grid density shall be used not only around study buildings but also around upstream buildings that might cause wake effects on the study building.
- Wind tunnel experimental data are indispensable for correct boundary prescription and validation of LES.
- The present study was limited to one wind direction, but as a part of the ongoing project, the authors are in the process of investigating wind directionality effects under an urban setting using a numerical approach. This investigation will be carried out using inhomogeneous inflow turbulence.

Acknowledgments

This research is based upon work supported by the *National Science Foundation* under Grant No. 0846811 and the Canada Research Chair support to the second author. Any opinions, findings, and conclusions or recommendations expressed in this material are those of the authors and do not necessarily reflect the views of the granting agencies.

References

ANSYS Inc. (2011), ANSYS FLUENT14 User's Guide. Ansys Inc., Southpoint 275 Technology Drive Canonsburg, PA.

ANSYS Inc. (2011), ANSYS ICEM CFD User Manual. Ansys Inc., Southpoint 275 Technology Drive Canonsburg, PA.

Batten, P., Goldberg, U. and Chakravarthy, S. (2004), “Interfacing statistical turbulence closures with large-eddy simulation”, *AIAA J.*, **42**(3), 485-492.

Bitsuamlak, G.T., Dagnew, A.K. and Chowdhury, A.G. (2010), “Computational assessment of blockage and wind simulator proximity effects for a new full-scale testing facility”, *Wind Struct.*, **13**(1), 21-36.

Billson, M., Eriksson, L.E. and Davidson, L. (2004), “Modeling of synthetic anisotropic turbulence and its sound emission”, *Proceedings of the 10th AIAA/CEAS Aeroacoustics Conference*, AIAA 2004- 2857, Manchester, United Kingdom.

Braun, A.L. and Awruch, A.M. (2009), “Aerodynamic and aeroelastic analyses on the CAARC standard tall building model using numerical simulation", *Comput. Struct*., **87**(9-10), 567-581.

COST (2007), Best practice guideline for the CFD simulation of flows in the urban environment COST Action 732.

Dagnew, A. and Bitsuamlak, G.T. (2013), "Computational evaluation of wind loads on buildings: a review", *Wind Struct.*, **16**(6), 629-660.

Dagnew A. and Bitsuamlak, G.T. (2010), "LES evaluation of external wind pressures on a standard tall building with and without a neighbouring building", *Proceedings of the 5th International Symposium on Computational Wind Engineering (CWE2010)*, May 2010.

Dagnew, A.K., Bitsuamalk, G.T. and Ryan, M. (2009), "Computational evaluation of wind pressures on tall buildings", *Proceedings of the 11th American Conference on Wind Engineering*, San Juan, Puerto Rico, June 20-26.

Davidson, L. (2007), "Using isotropic synthetic fluctuations as inlet boundary conditions for unsteady simulations", *Adv. Appl. Fluid Mech.*, **1**(1), 1-35.

Davidson, L. (2009), "Hybrid LES-RANS: back scatter from a scale-similarity model used as forcing", *Philos. T. R. Soc. A*, **367**, 2905-2915.

Franke. J. (2006), Recommendations of the COST action C14 on the use of CFD in predicting pedestrian wind environment.

Germano, M., Piomelli, U., Moin, P. and Cabot, W.H. (1996), "Dynamic subgrid-scale eddy viscosity model", *Proceedings of the Summer Workshop. Center for Turbulence Research*, Stanford, CA.

Huang, S., Li, Q.S. and Xu, S. (2007), "Numerical evaluation of wind effects on a tall steel building by CFD", *J. Constr. Steel Res*., **63**(5), 612-627.

Huang, S.H., Li, Q.S. and Wu, J.R. (2010), "A general inflow turbulence generator for large eddy simulation", *J. Wind Eng. Ind. Aerod.*, **98**(10-11), 600-617.

Huang, S.H. and Li, Q.S. (2010), "Large eddy simulation of wind effects on a super-tall building", *Wind Struct.*, **13**(6), 557-580.

Kataoka, H. and Mizuno, M., (2002), "Numerical flow computation around aeroelastic 3D square cylnder using inflow turbulence", *Wind Struct.*, **5** (2-4), 379-392.

Khanduri, A.C., Stathopoulos, T. and Bedard, C. (1998), "Wind-induced interference effects on buildings-a review of the state-of-art", *Eng. Struct.*, **20**, 617-630.

Kraichnan, R.H. (1970), "Diffusion by a random velocity field", *Phys. Fluids*, **13**(1), 22-31.

Lam, K.M. and To, A.P. (2006), "Reliability of numerical computation of pedestrian-level wind environment around a row of tall buildings", *Wind Struct.*, **9**(6), 473-492

Leonard, B.P. (1991), "The ultimate conservative difference scheme applied to unsteady one-dimensional advection", *Comput. Method. Appl. M.*, **88**(1), 17-74.

Lilly, D.K. (1992), "A Proposed Modification of the Germano subgrid-scale closure model", *Phys. Fluids*, **4**. 633-635.

Lund, T.S., Wu, X. and Squires, K.D. (1998), "Generation of turbulent inflow data for spatially-developing boundary layer simulations", *J. Comput. Phys.*, **140**, 233-258.

Martinuzzi, R. and Tropea, C. (1993), "The flow around surface-mounted, prismatic obstacles placed in a fully developed channel flow", *J. Fluids Eng. - T ASME*, **115**(1), 85-92.

Melbourne, W.H. (1980), "Comparison of measurements on the CAARC standard tall building model in simulated model wind flows", *J. Wind Eng. Ind. Aerod*., **6**(1-2), 73-88.

Murakami, S. (1998), "Overview of turbulence models applied in CWE–1997", *J. Wind Eng. Ind. Aerod*., **74-76**, 1-24.

Nozawa, K. and Tamura, T. (2002), "Large eddy simulation of the flow around a low-rise building immersed in a rough-wall turbulent boundary layer", *J. Wind Eng. Ind. Aerod*., **90**(10), 1151-1162.

Nozawa, K. and Tamura, T. (2003), "Numerical prediction of pressure on a high-rise building immersed in a turbulent boundary layer using LES", *Proceedings of the annual meeting of JACWE 95*.

Obasaju, E.D. (1992), "Measurement of forces and base overturning moments on the CAARC tall building model in a simulated atmospheric boundary layer", *J. Wind Eng. Ind. Aerod*., **40**(2), 103-126.

Sagaut, P. and Deck, S. (2009), "Large eddy simulation for aerodynamics: Status and perspectives", *Philos.*

T. R. Soc. A, **367**(1899), 2849-2860.

Senthooran, S., Lee, D. and Parameswaran, S. (2004), "A computational model to calculate the flow-induced pressure fluctuations on buildings", *J. Wind Eng. Ind. Aerod*., **92**(13), 1131-1145.

Shah, K.B. and Ferziger, J.H. (1997), *A fluid mechanics view of wind engineering: large eddy simulation of flow over a cubical obstacle,* (Eds., Meroney, R.N. and Bienkiewicz, B.), Computational Wind Engineering, 2, 211-226, Elsevier, Amsterdam.

Shinozuka M. (1985), *Lecture at CISM course on stochastic methods in structural engineering*, International Centre for Mechanical Science, Udine.

Simiu, E. and Scanlan, R.H. (1996), *Wind effects on structures*, John Wiley & Sons, New York, N.Y.

Smirnov, R., Shi, S. and Celik, I., (2001), "Random flow generation technique for large eddy simulations and particle-dynamics modeling", *J. Fluid. Eng. - T ASME* **123**(2), 359-371.

Swaddiwudhipong, S., Anh, T.T.T., Liu, Z.S. and Hua, J. (2007), "Modeling of wind load on single and staggered dual buildings", *Eng. Computers*, **23**(3), 215-22.

Tabor, G.D. and Baba-Ahmadi. M.H. (2009), "Inlet condition for large eddy simulation: a review", *Comput. Fluids*, **39** (4), 553-567.

Tamura, T. (2008), "Towards practical use of LES in wind engineering", *J. Wind Eng. Ind. Aerod*., **96**(10-11), 1451-1471.

Tamura, T., Nozawa, K. and Kondo, K. (2008), "AIJ guide for numerical prediction of wind loads on buildings", *J. Wind Eng. Ind. Aerod*., **96**(10-11), 1974-1984.

Tominaga, Y., Mochida, A., Murakami, S. and Sawaki, S. (2008), "Comparison of various revised k–ε models and LES applied to flow around a high-rise building model with 1:1:2 shape placed within the surface boundary layer", *J. Wind Eng. Ind. Aerod*., **96**(4), 389-411.

Tucker, P.G. and Lardeau, S. (2009), "Applied large eddy simulation", *Philos. T. R. Soc*., **367**(1899), 2809-2818.

Wright, N.G. and Easom, G.J. (2003), "Non-linear k–e turbulence model results for flow over a building at full-scale", *Appl. Math. Model.*, **27**(12), 1013-1033.

Zhang, A. and Gu, M. (2008), "Wind tunnel tests and numerical simulations of wind pressures on buildings in staggered arrangement", *J. Wind Eng. Ind. Aerod*., **96**(10-11), 2067-2079.

JH